Continuum modelling of orthotropic hexatruss lattice materials: effective stiffness and experimental validation

Federica Ongaro, Kévin Mathis, Frédéric Masson, Justin Dirrenberger

Continuum modelling of orthotropic hexatruss lattice materials: effective stiffness and experimental validation

Federica Ongaro, Kévin Mathis, Frédéric Masson, and Justin Dirrenberger

Abstract Architected materials are designed with specific configurations that offer enhanced properties, making them ideal for addressing various challenges in materials science, architecture, aerodynamics, and mechanical engineering. Their unique quality, coupled with the ability to tailor mechanical properties in every direction, renders them highly suitable for industries like aerospace, automotive, marine, and construction. However, the application of architected materials depends on the development of accurate models to understand the complex relationship between microstructure characteristics and macroscopic behavior. Despite the proposal and discussion of numerous analytical and numerical methods in recent years, very few studies have derived explicit formulas for effective mechanical properties. This paper contributes to this underexplored area by presenting a mathematical formulation and modeling technique for the effective elastic moduli of a three-dimensional orthotropic hexatruss lattice. The analytical relations we have established, validated through comprehensive experimental tests on a 3D-printed lattice, demonstrate the significant impact of lattice parameters on macroscopic properties. Practically, our results could simplify the process of parametric optimization for architectured materials, offering a less resource-intensive approach to optimization since parameter changes do not necessitate lattice regeneration.

Federica Ongaro and Justin Dirrenberger
PIMM Lab, Arts et Métiers, Cnam, CNRS UMR 8006, 151 Bd de l'Hôpital, 75013 Paris, France
e-mail: federica.ong@gmail.com ; justin.dirrenberger@ensam.eu

Kévin Mathis and Frédéric Masson
CNES-Launchers Directorate, 52 Rue Jacques Hillairet, 75612 Paris Cedex, France e-mail: kevin.mathis@cnes.fr ; frederic.masson@cnes.fr

1 Introduction

1.1 Architectured materials: overview

Architectured materials, composed of two or more materials and/or spaces [Ashby, 2013], offer a unique blend of mechanical properties such as stiffness, strength, and toughness at a lower density. This combination allows for previously conflicting performances to coexist within a single homogeneous material.

Their distinctive configuration, resulting from their discrete nature, makes architectured materials highly suitable for engineering applications across various industries, including aerospace, automotive, marine, and construction. For instance, the light weight of microtrusses or lattice structures is perfect for core materials in lightweight, high-performance sandwich panels in aerospace components and sports equipment. Additionally, their low compressive strength coupled with high deformation capacity makes them excellent for shock mitigation and energy absorption in impulsive events [D'Mello and Waas, 2013].

However, their application hinges on the development of suitable constitutive models to uncover their effective properties. Two sets of parameters influence their mechanical behavior: one relates to the material composition, and the other to the geometric and topological characteristics of the microstructure. Transitioning from a microscopic discrete description to a coarse continuous model is challenging. To address this, concepts of energy equivalence and micro-to-macro force and displacement relations are typically employed. Common simplifications like linear elasticity, material isotropy, and the assumption that the microstructure behaves according to classical beam theory are often used. These simplifications provide explicit stress-strain relations and aid in understanding the fundamental mechanical aspects of these materials.

1.2 State of the art

A significant number of researchers have explored the mechanical modeling of architectured materials, leading to a diverse array of techniques that have been extensively discussed in recent literature. Key contributions, offering various methods and assumptions, can be found in the review papers authored by Christensen [2000], Kraynik et al. [1998], Warren and Kraynik [1997]. Additionally, the technical details concerning the analysis of structural lattices and the formulation of their equivalent constitutive equations have been comprehensively reviewed by [Ostoja-Starzewski, 2002]. This review also includes a comprehensive list of references for further reading and study.

The most recognized and extensively utilized micromechanical model in the field of architectured materials is attributed to the groundbreaking work of Gibson [1989], Gibson and Ashby [1999]. Their research primarily concentrated on the deforma-

tion mechanism of a single cell when subjected to various types of external loads. Specifically, Gibson and colleagues derived first-order power-law relations that link the parameters of the microstructure with the macroscopic properties of a broad spectrum of architectured materials. This was achieved by assuming infinitesimal strains and employing standard beam theory to model the edges of the lattice structure.

Chen et al. [1998] and Kumar and McDowell [2004] proposed an alternative methodology to address the critical transition from microscale to macroscale and to formulate the constitutive model for two-dimensional microstructures undergoing in-plane deformations. Similar to the approach by [Gibson, 1989, Gibson and Ashby, 1999], their method also idealizes the discrete lattice as a series of Euler-Bernoulli beams. The macroscopic description in their approach is derived using an energy-based technique.

In the context of homogenization theory, Gonella and Ruzzene [2008] adopted a unique approach by interpreting the discrete lattice through the lens of finite difference formalism. This method involves applying Taylor's series expansions to the nodal displacements and rotations. This technique is particularly motivated by the multi-scale nature of the problem being addressed, allowing for a more accurate representation of the behavior of the discrete lattice when transitioning to an equivalent continuum model.

The application of crystal theory, as outlined by [Brillouin, 1953], was instrumental for researchers like [Hutchinson and Fleck, 2006, Elsayed and Pasini, 2010, Vigliotti and Pasini, 2012b], in estimating the effective stiffness of various two-dimensional lattice materials. These materials were modeled as pin-jointed, infinite microtruss structures created by tessellating a unit cell into a periodic modular pattern. The approach they employed is based on the Cauchy-Born assumption [Born and Huang, 1954]. This assumption allows for the expression of the lattice's nodal displacements in terms of the macroscopic strain field applied. From this, the homogenized properties of the lattice material can be derived, effectively linking the microscale structure to its macroscopic mechanical behavior.

The mechanical behavior of three-dimensional lattice materials has also been studied using force- and energy equivalence-based techniques. Zhu et al. [1997], for instance, formulated the Young's modulus, shear modulus, and Poisson's ratio of the tetrakaidecahedral lattice in terms of its relative density. Furthermore, the mechanical performance of the octet-truss lattice has been explored both theoretically and numerically, as detailed in [Deshpande et al., 2001, Challapalli, 2020]. These studies not only derived the effective elastic properties of the lattice but also established collapse surfaces for buckling and plastic yielding. The validity of these findings was further reinforced through experimental observations, ensuring a comprehensive understanding of the lattice's mechanical performance.

A broader examination of three-dimensional periodic lattices is presented in [Vigliotti and Pasini, 2012a, Refai et al., 2020, Albertini et al., 2019, 2021]. These authors utilized a finite element-based homogenization method to evaluate the macroscopic elastic properties of both open- and closed-cell lattices. Their studies focused on various well-known topologies of the unit cell, such as Body-Centered Cubic (BCC), Face-Centered Cubic (FCC), and octet structures. This approach allowed

for a detailed and comprehensive understanding of how different lattice topologies influence the overall elastic properties of the material.

1.3 Scope and outline of the present paper

Though the above-mentioned authors numerically and theoretically analysed the mechanical behavior of architectured materials, up to date closed-form expressions for the effective elastic moduli have been derived in a very limited number of cases. To make a contribution to this incomplete research area and to provide some useful tools for practical applications, this paper suggests a modelling technique to derive explicit relations for the macroscopic elastic properties of orthotropic hexatruss lattice materials which were initially introduced by Dirrenberger et al. [2013] for the cubic case, although not yet studied in the literature for the orthotropic case. For the sake of conciseness, we focused in this work on the stiffness in the three principal directions, as we could measure them experimentally and were of interest for the industrial application considered in this work.

The work is organised in 4 sections, including this introduction. Initially, by modelling the examined lattice as a sequence of three-dimensional Euler-Bernoulli beams, an energy-based approach coupled with the Cauchy-Born assumption provide, in Section 2, closed-form expressions for the macroscopic elastic moduli. The outcome of the experimental campaign to verify the derived analytical equations is described in Section 3. A very good agreement generally emerges. Finally, Section 4 summarises the main findings. This paper is an extension of the previously available conference paper [Ongaro et al., 2019].

2 The hexatruss lattice: theoretical modelling and homogenization of the discrete system

2.1 Problem statement

This paper focuses on the three-dimensional auxetic microstructure presented by Dirrenberger et al. [2013], generated by tessellating a hexatruss unit cell (Figure 1) through the space along three independent periodic vectors, $\mathbf{l}_1$, $\mathbf{l}_2$ and $\mathbf{l}_3$. In the global reference system, defined by the unit orthonormal vectors $\boldsymbol{e}_1$, $\boldsymbol{e}_2$, $\boldsymbol{e}_3$ and by the coordinate system (X, Y, Z), the components of the lattice vectors are

$$\mathbf{l}_1 = \begin{bmatrix} L_1 & 0 & 0 \end{bmatrix}^T, \quad \mathbf{l}_2 = \begin{bmatrix} 0 & L_2 & 0 \end{bmatrix}^T, \quad \mathbf{l}_3 = \begin{bmatrix} 0 & 0 & L_3 \end{bmatrix}^T, \tag{1}$$

with L_1, L_2, L_3 the overall dimensions of the cell (the lattice size) in the directions $\boldsymbol{e}_1$, $\boldsymbol{e}_2$, $\boldsymbol{e}_3$, respectively.

The resulting system can be conceived as a collection of discrete elements connected at nodes locations periodically arranged. In particular, two classes of nodes can be identified: the internal nodes and the boundary nodes. The first connect elements of only a single cell while the second connect elements of confining cells. Also, due to the periodicity of the lattice configuration, the boundary nodes are corresponding along the lattice vectors and, as outlined in the following sections, such nodes will be subjected to the imposition of appropriate constraints in order to preserve the periodicity of the deformed lattice.

Finally, from a mechanical point of view, the examined microstructure is treated as an interconnected network of three-dimensional Euler-Bernoulli beams having circular cross-section of radius r and made of a linear elastic, homogeneous and isotropic material with Young modulus E_s, Poisson ration ν_s and shear modulus G_s.

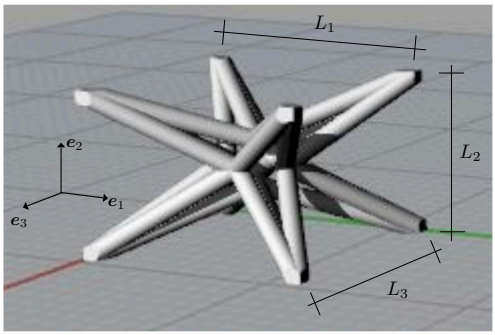

Fig. 1 The hexatruss unit cell

2.2 Continuum modelling

2.2.1 Overview

At the macroscopic scale, the effective properties of a lattice material can be derived from the geometric and mechanical parameters of the microstructure. However, analysing large size volumes on a microstructural level to gain an accurate estimation of the local fields is unsuitable and, in some cases, may involve considerable efforts. Thus, the typical approach to the continuum modelling of architectured materials includes the selection of a *Representative Volume Element* (RVE) that is then subjected to the imposition of appropriate boundary conditions to model different loading situations.

By decomposing the displacement field on the material points of the RVE, $\boldsymbol{x} \in V$, into the main part $\mathbf{E} \cdot \boldsymbol{x}$ and the zero-mean fluctuation part $\boldsymbol{u}^*$,

$$\boldsymbol{u} := \mathbf{E} \cdot \boldsymbol{x} + \boldsymbol{u}^*, \qquad \forall \boldsymbol{x} \in V, \tag{2}$$

with

$$\mathbf{E} := \begin{bmatrix} E_{11} & E_{12} & E_{13} \\ E_{12} & E_{22} & E_{23} \\ E_{13} & E_{23} & E_{33} \end{bmatrix} \tag{3}$$

the macroscopic strain tensor, periodic conditions enforce the periodicity of the fluctuation field and the anti-periodicity of the traction field $\boldsymbol{t}$ on the RVE's boundary. Namely,

$$\begin{cases} \boldsymbol{u}_+^* = \boldsymbol{u}_-^*, & \forall \boldsymbol{x}_+ \in \partial V_+ \text{ and matching } \boldsymbol{x}_- \in \partial V_-, \\ \boldsymbol{\Sigma} \cdot \boldsymbol{n}_+ := \boldsymbol{t}_+ = \boldsymbol{t}_- =: \boldsymbol{\Sigma} \cdot \boldsymbol{n}_-, & \forall \boldsymbol{x}_+ \in \partial V_+ \text{ and matching } \boldsymbol{x}_- \in \partial V_-, \\ \partial V_+ \cup \partial V_- = \partial V, \\ \partial V_+ \cap \partial V_- = \varnothing, \end{cases} \tag{4}$$

where $\boldsymbol{n}_+$ and $\boldsymbol{n}_-$ stand, respectively, for the unit normal to ∂V_+ and ∂V_-,

$$\boldsymbol{\Sigma} := \begin{bmatrix} \Sigma_{11} & \Sigma_{12} & \Sigma_{13} \\ \Sigma_{12} & \Sigma_{22} & \Sigma_{23} \\ \Sigma_{13} & \Sigma_{23} & \Sigma_{33} \end{bmatrix} \tag{5}$$

the macroscopic stress tensor.

Periodic boundary conditions will be selected in Section 2.3.3 to investigate the mechanical response of the examined microstructure, whose periodic configuration allows us to identify the RVE with the repetitive unit cell of the tessellation [Nemat-Nasser and Hori, 1993].

2.2.2 The hexatruss unit cell as RVE: geometric description and energetics

The hexatruss unit cell is composed by the eight boundary nodes 1, 2, 3, 4, 5, 6, 7, 8 linked to the internal ones 9, 10, 11, 12, 13, 14 by the line elements

$$1-9,\ 2-9,\ 6-9,\ 5-9 \qquad \text{(Face Front)}$$

$$4-10,\ 3-10,\ 7-10,\ 8-10 \qquad \text{(Face Back)}$$

$$1-11,\ 2-11,\ 3-11,\ 4-11 \qquad \text{(Face Bottom)}$$

$$5-12,\ 6-12,\ 7-12,\ 8-12 \qquad \text{(Face Top)}$$

$$1-13,\ 4-13,\ 8-13,\ 5-13 \qquad \text{(Face Left)}$$

$$2-14,\ 3-14,\ 7-14,\ 6-14 \qquad \text{(Face Right)}$$

that, in the global reference system ($\boldsymbol{e}_1$, $\boldsymbol{e}_2$, $\boldsymbol{e}_3$), are described by the vectors

$$\mathbf{b}_{A-B} = \mathbf{p}_B - \mathbf{p}_A, \tag{6}$$

with $\mathbf{p}_A$ and $\mathbf{p}_B$, respectively, the position vectors of the extreme nodes of the element, A and B the index listed in Table 1. For sake of clarity, it is worth noting that, in Equation (6), $\mathbf{p}_A$ and $\mathbf{p}_B$ are expressed in the global reference system so that, to differentiate the global variables from the local ones (cf. Section 2.2), uppercase letters, i.e., indices A and B, are used. For the interested reader, the components of the $\mathbf{b}_{A-B}$ vectors are listed in Appendix A.

As anticipated in Section 2.1, from a mechanical point of view, the connecting elements are represented as three-dimensional Euler-Bernoulli beams and this assumption, along with an energy-based approach, lead to closed-form expressions for the effective elastic moduli of the examined lattice material.

Specifically, in terms of energy, for any given deformation the elastic energy representative of the whole discrete structure, W, can be evaluated from that of the beams composing the unit cell of the periodic array. Namely, after writing the equation for the elastic strain energy of the Euler-Bernoulli beam in the global reference system and summing the energetic contribution of each beam, it emerges

$$W = \frac{1}{2}\mathbf{D}^T \cdot \mathbf{K}\mathbf{D}, \tag{7}$$

with

$$\mathbf{D} := \begin{bmatrix} \mathbf{D}_1 \\ \mathbf{D}_2 \\ \cdots \\ \mathbf{D}_{14} \end{bmatrix} = \begin{bmatrix} U_1 & V_1 & W_1 & \Phi_{X1} & \Phi_{Y1} & \Phi_{Z1} & \cdots & \Phi_{Z14} \end{bmatrix}^T \tag{8}$$

the global displacements vector, collecting the displacements and rotations of all nodes of the unit cell and $\mathbf{K}$ the global stiffness matrix, assembled by adopting standard techniques of the finite element method [Ferreira, 2009].

2.2.3 Elastic energy and effective moduli of the equivalent continuum

The continuum form of W can be derived by adopting the Cauchy-Born relation [Vigliotti and Pasini, 2012c,a], providing a viable approach to express the displacements of each node of the unit cell as a function of the macroscopic strain field applied, $\mathbf{E}$.

Specifically, if we introduce the vector $\mathbf{D}_R$ collecting the displacements of the generic R-th node within the cell and the corresponding position vector $\mathbf{p}_R$, the Cauchy-Born relation, in its general form, can be expressed as

$$\mathbf{D}_R = \mathbf{D}_0 + \mathbf{E} \cdot (\mathbf{p}_R - \mathbf{p}_0), \tag{9}$$

with $\mathbf{D}_0$ and $\mathbf{p}_0$, in turn, the displacements vector and position vector of an appropriately selected unit cell's independent node. Also, by enforcing the equilibrium conditions on the nodal forces [Vigliotti and Pasini, 2012b], it is possible to calculate the displacements $\mathbf{D}_0$ in terms of $\mathbf{E}$.

Notwithstanding alternative choices of the independent node are possible [Vigliotti and Pasini, 2012a], in this work the boundary node 4 has been selected as independent node, leading to

$$\mathbf{D}_R = \mathbf{D}_4 + \mathbf{E} \cdot (\mathbf{p}_R - \mathbf{p}_4), \qquad R = 1, 2, ..., 14. \tag{10}$$

This assumption provides an easy way to impose kinematic conditions on the boundary nodes of the cell,

$$\begin{aligned} \mathbf{D}_1 &= \mathbf{D}_4 + \mathbf{E} \cdot \mathbf{l}_3, & \mathbf{D}_2 &= \mathbf{D}_4 + \mathbf{E} \cdot (\mathbf{l}_1 + \mathbf{l}_3), \\ \mathbf{D}_3 &= \mathbf{D}_4 + \mathbf{E} \cdot \mathbf{l}_1, & \mathbf{D}_5 &= \mathbf{D}_4 + \mathbf{E} \cdot (\mathbf{l}_2 + \mathbf{l}_3), \\ \mathbf{D}_6 &= \mathbf{D}_4 + \mathbf{E} \cdot (\mathbf{l}_1 + \mathbf{l}_2 + \mathbf{l}_3), & & \\ \mathbf{D}_7 &= \mathbf{D}_4 + \mathbf{E} \cdot (\mathbf{l}_1 + \mathbf{l}_2), & \mathbf{D}_8 &= \mathbf{D}_4 + \mathbf{E} \cdot \mathbf{l}_2, \end{aligned} \tag{11}$$

that coincide, as anticipated in Section 2.2.1, with the application of periodic boundary conditions in order to enforce the periodicity of the deformed configuration.

Substituting Equation (10) into (7) and dividing the expression that turns out from the calculation by the volume of the unit cell, $V = L_1 L_2 L_3$, give the strain energy density in the continuum approximation, w. It emerges that w is a quadratic form of the infinitesimal strains E_{ij},

$$w = w\left(E_{ij}\right), \quad i, j = 1, 2, 3, \tag{12}$$

and, as in classical continuum mechanics, evaluating the Hessian of the strain energy density with respect to the deformation components enables to derive the entries

$$C_{ijkl} = \frac{\partial^2 w}{\partial E_{ij}\, \partial E_{kl}}, \quad i, j, k, l = 1, 2, 3 \tag{13}$$

of the fourth-order tensor of effective elastic moduli of the lattice, $\boldsymbol{C}$, that relates the macroscopic stress, Σ_{ij}, and strain, E_{ij}, components as follows:

$$\Sigma_{ij} = C_{ijkl} E_{kl}, \quad i, j, k, l = 1, 2, 3. \tag{14}$$

Using Voigt's notation, the effective elastic moduli depending on the geometrical and mechanical parameters of the microstructure can be derived:

$$C_{ij} = C_{ij}\left(E_s,\, \nu_s,\, L_1,\, L_2,\, L_3,\, r,\, d_1,\, d_2,\, d_3\right), \quad i, j = 1, 2, ..., 6, \tag{15}$$

with E_s and ν_s the mechanical characteristics of the constituent material, r the radius of the beams' cross-section, L_k and d_k, $k = 1, 2, 3$.

The effective moduli to be considered correspond to the principal directions of the cell $\boldsymbol{e}_1, \boldsymbol{e}_2, \boldsymbol{e}_3$:

$$C_X := C\left(\boldsymbol{e}_1\right), \qquad C_Y := C\left(\boldsymbol{e}_2\right), \qquad C_Z := C\left(\boldsymbol{e}_3\right), \tag{16}$$

where, for sake of clarity, the subscripts X, Y, Z have been used to denote the effective principal stiffness, $C_{(\cdot)}$, with reference to the axes $\boldsymbol{e}_1$, $\boldsymbol{e}_2$, $\boldsymbol{e}_3$.

It emerges that the microstructural parameters strongly affect the effective properties listed in Equation (16) and also in this case explicit relations, reported in Appendix B, can be obtained:

$$\begin{aligned}
C_X &= \frac{\partial^2 w}{\partial E_{11}\,\partial E_{11}} = C_X\left(E_s,\, \nu_s,\, L_1,\, L_2,\, L_3,\, r,\, d_1,\, d_2,\, d_3\right), \\
C_Y &= \frac{\partial^2 w}{\partial E_{22}\,\partial E_{22}} = C_Y\left(E_s,\, \nu_s,\, L_1,\, L_2,\, L_3,\, r,\, d_1,\, d_2,\, d_3\right), \\
C_Z &= \frac{\partial^2 w}{\partial E_{33}\,\partial E_{33}} = C_Z\left(E_s,\, \nu_s,\, L_1,\, L_2,\, L_3,\, r,\, d_1,\, d_2,\, d_3\right).
\end{aligned} \tag{17}$$

From this point of view, the advantage of the proposed theory is that an explicit relation between the microstructural parameters and the macroscopic moduli can be obtained. In a practical context, this offers three advantages. Firstly, a full understanding of the interplay between the macroscopic properties and the underlying microstructure, suggesting an alternative route to the time-consuming experimental investigations for predicting the macroscopic stiffness. Secondly, an assistance for the designer in the selection of the microstructural parameters, dimension of the unit cell, radius of the beams' cross-section, position of the internal nodes, in order to reach a prescribed value of macroscopic stiffness. Finally, the possibility to formulate a more efficient and less computationally expensive optimization problem in order to derive the microstructural parameters satisfying a given set of stiffness requirements. In particular, the optimization problem that would be established would coincide with the optimization of the analytical expressions in Equation (17) so that, to evaluate the optimal parameters, the re-generation and corresponding analysis of the lattice are not required at each iteration.

3 Validation of the theoretical results by experimental confrontation

In this section, the analytical results proposed in Equation (17) are verified by comparison with those obtained by performing experimental tests.

To further establish the validity of the proposed modelling approach, the theoretical findings in Equation (17) are compared with the outcome of the experimental tests presented in the following.

Also in this case, for simplicity, we will refer to E_X, E_Y and E_Z as the apparent Young moduli of the lattice along the principal directions of the unit cell, $\boldsymbol{e}_1$, $\boldsymbol{e}_2$ and

$\boldsymbol{e}_3$, making the assumption that the effective elastic moduli in principal directions defined in Section 2.2.3 are similar in value to the experimentally measured Young moduli, therefore assuming a Poisson ratio close to zero, which is reasonable in the principal direction for an hexatruss lattice Dirrenberger et al. [2013].

3.1 Description of the samples

The mechanical tests have been conducted on 3D-printed 3×3×3 unit cell hexatruss lattices and, to obtain an estimation of the effective stiffness in the directions $\boldsymbol{e}_1$, $\boldsymbol{e}_2$ and $\boldsymbol{e}_3$, three configurations have been investigated (Figure 2):

- Configuration $C1$: to consider the direction $\boldsymbol{e}_1$ and derive E_X,
- Configuration $C2$: to consider the direction $\boldsymbol{e}_2$ and derive E_Y,
- Configuration $C3$: to consider the direction $\boldsymbol{e}_3$ and derive E_Z.

Aiming at obtaining a good quality of the printed samples, a unit cell with overall dimensions

$$L_1 = 9.6\,\text{mm}, \qquad L_2 = 11.52\,\text{mm}, \qquad L_3 = 7.68\,\text{mm} \tag{18}$$

has been selected, leading to

- Configuration $C1$ (length × width × height): 34.56 mm × 23.04 mm × 28.8 mm,
- Configuration $C2$ (length × width × height): 28.8 mm × 23.04 mm × 34.56 mm,
- Configuration $C3$ (length × width × height): 28.8 mm × 34.56 mm × 23.04 mm.

In terms of radius of the beams' cross-section, r, and position of the internal nodes, parameters d_1, d_2 and d_3, the following values have been adopted:

$$\begin{gathered} r = 0.45\,\text{mm}, \\ d_1 = 2.8\,\text{mm}, \quad d_2 = 2.2\,\text{mm}, \quad d_3 = 3.3\,\text{mm}. \end{gathered} \tag{19}$$

Regarding the constituent material, two different polymers have been used to print the samples: PLA (Polylactic Acid) and PET (Polyethylene Terephthalate) having, on order, Young modulus of

$$E_{PLA} = 1.3\,\text{GPa}, \qquad E_{PET} = 0.8\,\text{GPa}, \tag{20}$$

values obtained by conducting traction tests according to the ASTM D638-14 standard [ASTM, 2014]. Also, as suggested in the literature [Seitz, 1993, Ferreira et al., 2017], a Poisson ratio of

$$\nu_{PLA} = 0.33, \qquad \nu_{PET} = 0.43\,\text{GPa} \tag{21}$$

has been respectively assumed.

Finally, to account for possible errors associated with the 3D-printing process, three copies of each configuration have been printed and tested.

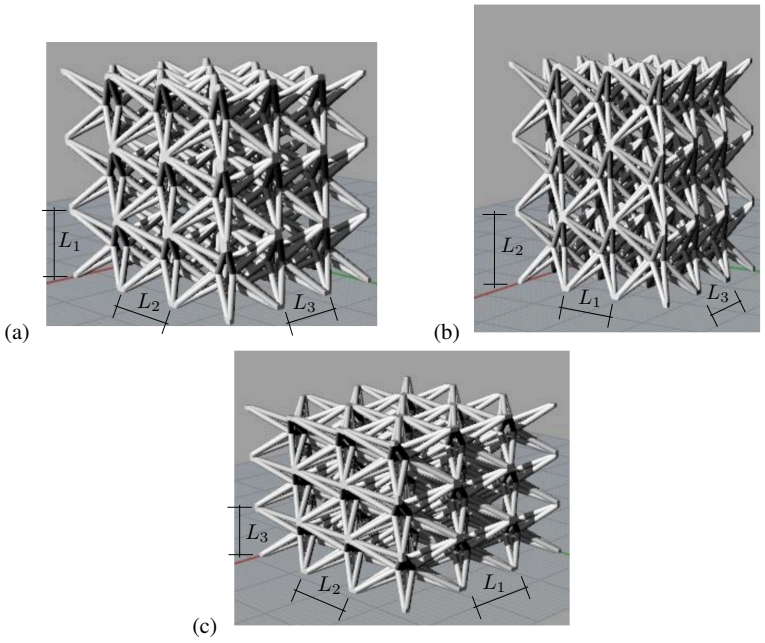

Fig. 2 The three different configurations of the samples involved in the mechanical tests: (a) configuration C1, (b) configuration C2, (c) configuration C3

3.2 Type of tests

To characterise the 3D-printed samples, the following mechanical tests have been performed (Figure 3):

- uniaxial compression tests at room temperature,
- displacement-controlled tests at a displacement rate of 0.5 mm/min,
- only elastic deformations involved, $\varepsilon_{max} = 1\,\%$,
- no interfaces between the sample and the test bench,
- no constraints applied to movement (lateral displacements allowed)

and the testing machine *Instron 5881* has been employed.

3.3 Methodology adopted

As anticipated in Section 3.2.1, the aim of the tests was to evaluate the effective stiffness of the hexatruss lattice in the three principal directions of the unit cell, $\boldsymbol{e}_1$, $\boldsymbol{e}_2$ and $\boldsymbol{e}_3$, obtained by analysing the force-displacement and stress-strain curves experimentally obtained.

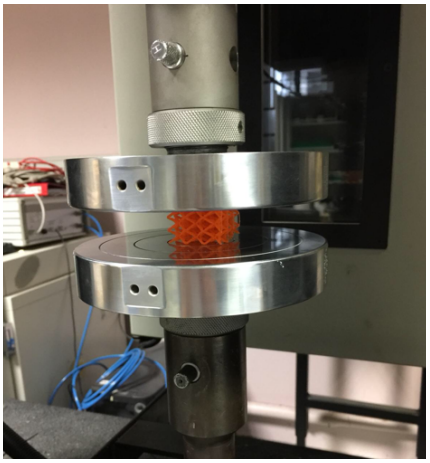

Fig. 3 Experimental validation: compression tests

The force-displacement curves, in particular, have been derived by recording, during the test, both the displacement, ΔL_{Ci}, $i = 1, 2, 3$, and resulting load, F_{Ci}, $i = 1, 2, 3$, applied to the sample. By knowing the sample geometry, it was then possible to generate the stress-strain curves, being the engineering strain, ε_{Ci}, and the engineering stress, σ_{Ci}, given by

$$\varepsilon_{Ci} := \frac{\Delta L_{Ci}}{L_{Ci}} \quad \text{and} \quad \sigma_{Ci} := \frac{F_{Ci}}{A_{Ci}}, \quad i = 1, 2, 3, \tag{22}$$

with L_{Ci} and A_{Ci}, in turn, the initial height of the sample and its initial cross-sectional area normal to the loading direction.

Finally, since we are working in a linear elastic regime, the slope of the stress-strain curves provides the Young moduli E_{C1}, E_{C2}, E_{C3} corresponding to the three configurations tested $C1$, $C2$, $C3$:

$$E_{C1} := \frac{\sigma_{C1}}{\varepsilon_{C1}}, \quad E_{C2} := \frac{\sigma_{C2}}{\varepsilon_{C2}}, \quad E_{C3} := \frac{\sigma_{C3}}{\varepsilon_{C3}}. \tag{23}$$

As stated, for simplicity, they are assumed to coincide with the effective Young moduli of the lattice along its principal directions $\boldsymbol{e}_1$, $\boldsymbol{e}_2$, $\boldsymbol{e}_3$:

$$E_{C1} \equiv E_X, \quad E_{C2} \equiv E_Y, \quad E_{C3} \equiv E_Z. \tag{24}$$

3.4 Results and discussion

The outcome of the experimental campaign is gathered in Appendix C as Figures 4 and 5, in terms of force-displacement curves, and in Figures 6 and 7, in terms of

stress-strain curves. The derived Young moduli are reported in Tables 1 and 2, where the comparison between the experimental results and the theoretical predictions in Equation (17) is also included.

It should be noted that the curves illustrated in Figures 4-7 and the experimental values listed in Tables 1 and 2 represent, for each configuration, the average response of the three samples tested (cf. Section 3.2.1). Also, in Tables 1 and 2, the analytical values are obtained by substituting into Equation (17) the parameters listed in Equations (18), (19) and the material properties, that coincide with the geometrical and mechanical characteristics of the unit cell adopted in the experimental tests.

As it can be seen, it generally emerges a good agreement between the theoretical and experimental results and, as expected, the theoretical values overestimate the experimental ones of averagely 2-3 %. From this point of view, the difference is mainly related to the quality of the 3D-printed samples that, differently from the analytical model where the beams are assumed to be perfectly homogeneous and without defects, in some cases present some imperfections, i.e., small parts missing, not perfectly homogeneous or beams not perfectly connected at the nodes.

However, taking into account the very close comparison in Tables 1 and 2, it can be said that the experimental tests confirm the validity of our modelling strategy. This can also be observed in Figures 6 and 7, where the experimental stress-strain curves are compared with the theoretical ones. The latter, in particular, are obtained from the analytical values of Table 1, Figure 6, and Table 2, Figure 7.

Table 1 PLA samples, Young's moduli. Comparison between the theoretical and experimental results

	Experiments	Theoretical results
E_X (MPa)	2.72 ± 0.34	3.09
E_Y (MPa)	4.55 ± 0.25	4.79
E_Z (MPa)	1.32 ± 0.11	1.34

Table 2 PET samples, Young's moduli. Comparison between the theoretical and experimental results

	Experiments	Theoretical results
E_X (MPa)	1.81 ± 0.10	1.90
E_Y (MPa)	2.71 ± 0.17	2.95
E_Z (MPa)	0.90 ± 0.04	0.92

4 Conclusions

Architectured materials, due to their discrete configuration, present enhanced mechanical properties such as stiffness, strength, and toughness at a lower density. This unique attribute, combined with the ability to customize their mechanical properties, renders them highly promising for a wide range of engineering applications, including aerospace, automotive, marine, and construction sectors. Unlike traditional homogeneous materials, architectured materials necessitate specialized constitutive models to elucidate the intricate relationship between microstructural parameters and macroscopic properties. Although various techniques and methods have been proposed in recent literature, only a few studies offer closed-form expressions for the effective mechanical properties. These expressions are crucial for designers to select materials that best meet specific requirements.

Addressing this research gap, this paper focuses on the analysis of a three-dimensional orthotropic lattice composed of hexatruss cells. Using linear elasticity and modeling the microstructure as a series of three-dimensional Euler-Bernoulli beams, an energetic approach yields explicit expressions for effective stiffness. The Cauchy-Born assumption simplifies the problem mathematically by representing the nodal degrees of freedom in terms of the applied macroscopic strain components. This transforms the elastic energy of the discrete system into a quadratic function of these components, allowing for the derivation of the macroscopic stiffness tensor and corresponding elastic moduli, akin to classical mechanics. The theoretical predictions are validated through mechanical tests on 3D-printed lattices.

A notable advantage of the theoretical approach in this paper is its extensibility to different types of periodic lattices, which can be achieved by tessellating various unit cells or using different beam models, such as the Timoshenko beam. Moreover, the analytical expressions derived can lead to a more efficient parametric optimization problem for architectured materials. Unlike existing literature, this approach does not necessitate the computationally intensive and time-consuming regeneration and analysis of the lattice when parameters are altered.

Appendix A

In the global reference system ($\boldsymbol{e}_1$, $\boldsymbol{e}_2$, $\boldsymbol{e}_3$), the components of the $\mathbf{b}_{A-B}$ vectors introduced in Section 2.3 are

$$\mathbf{b}_{1-9} = \begin{bmatrix} L_1/2 \\ L_2/2 \\ -d_1 \end{bmatrix}, \quad \mathbf{b}_{2-9} = \begin{bmatrix} -L_1/2 \\ L_2/2 \\ -d_1 \end{bmatrix}, \quad \mathbf{b}_{6-9} = \begin{bmatrix} -L_1/2 \\ -L_2/2 \\ -d_1 \end{bmatrix}, \quad \mathbf{b}_{5-9} = \begin{bmatrix} L_1/2 \\ -L_2/2 \\ -d_1 \end{bmatrix},$$

$$\mathbf{b}_{4-10} = \begin{bmatrix} L_1/2 \\ L_2/2 \\ d_1 \end{bmatrix}, \quad \mathbf{b}_{3-10} = \begin{bmatrix} -L_1/2 \\ L_2/2 \\ d_1 \end{bmatrix}, \mathbf{b}_{7-10} = \begin{bmatrix} -L_1/2 \\ -L_2/2 \\ d_1 \end{bmatrix}, \mathbf{b}_{8-10} = \begin{bmatrix} L_1/2 \\ -L_2/2 \\ d_1 \end{bmatrix},$$

$$\mathbf{b}_{1-11} = \begin{bmatrix} L_1/2 \\ d_2 \\ -L_3/2 \end{bmatrix}, \mathbf{b}_{2-11} = \begin{bmatrix} -L_1/2 \\ d_2 \\ -L_3/2 \end{bmatrix}, \mathbf{b}_{3-11} = \begin{bmatrix} -L_1/2 \\ d_2 \\ L_3/2 \end{bmatrix}, \quad \mathbf{b}_{4-11} = \begin{bmatrix} L_1/2 \\ d_2 \\ L_3/2 \end{bmatrix},$$

$$\mathbf{b}_{5-12} = \begin{bmatrix} L_1/2 \\ -d_2 \\ -L_3/2 \end{bmatrix}, \mathbf{b}_{6-12} = \begin{bmatrix} -L_1/2 \\ -d_2 \\ -L_3/2 \end{bmatrix}, \mathbf{b}_{7-12} = \begin{bmatrix} -L_1/2 \\ -d_2 \\ L_3/2 \end{bmatrix}, \quad \mathbf{b}_{8-12} = \begin{bmatrix} L_1/2 \\ -d_2 \\ L_3/2 \end{bmatrix},$$

$$\mathbf{b}_{1-13} = \begin{bmatrix} d_3 \\ L_2/2 \\ -L_3/2 \end{bmatrix}, \quad \mathbf{b}_{4-13} = \begin{bmatrix} d_3 \\ L_2/2 \\ L_3/2 \end{bmatrix}, \quad \mathbf{b}_{8-13} = \begin{bmatrix} d_3 \\ -L_2/2 \\ L_3/2 \end{bmatrix}, \mathbf{b}_{5-13} = \begin{bmatrix} d_3 \\ -L_2/2 \\ -L_3/2 \end{bmatrix},$$

$$\mathbf{b}_{2-14} = \begin{bmatrix} -d_3 \\ L_2/2 \\ -L_3/2 \end{bmatrix}, \quad \mathbf{b}_{3-14} = \begin{bmatrix} -d_3 \\ L_2/2 \\ L_3/2 \end{bmatrix}, \quad \mathbf{b}_{7-14} = \begin{bmatrix} -d_3 \\ -L_2/2 \\ L_3/2 \end{bmatrix}, \mathbf{b}_{6-14} = \begin{bmatrix} -d_3 \\ -L_2/2 \\ -L_3/2 \end{bmatrix}, \tag{25}$$

with L_1, L_2, L_3, in turn, the dimensions of the unit cell in the directions $\boldsymbol{e}_1$, $\boldsymbol{e}_2$, $\boldsymbol{e}_3$ and d_1, d_2, d_3 the parameters specifying the position of the internal nodes.

Appendix B

The complete expressions of the effective elastic moduli in the directions $\boldsymbol{e}_1$, $\boldsymbol{e}_2$ and $\boldsymbol{e}_3$ have been derived using Matlab, and are respectively,

$$\begin{aligned} C_X &= p_{12}\left(\left(AL_1^2 p_5 + 48I\left(p_6 + 4d_2^2 p_1^{5/2}\right)\right) p_3^{5/2} + 64\, d_3^6 A\,(p_1 p_2)^{5/2} + d_3^4 p_4\,(16A + 192I)\right) E_s, \\ C_Y &= p_{12}\left(4d_3^2\left(48I + AL_2^2\right)(p_1 p_2)^{5/2} + 48I p_7 + A\,(p_8 + p_9)\right) E_s, \\ C_Z &= p_{12}\left(192 d_3^2 I\,(p_1 p_2)^{5/2} + A\, p_1\, p_2\, p_3\, p_{10} + 48I p_{11}\right) E_s, \end{aligned} \tag{26}$$

where, to simplify the notation, $A := \pi r^2$, $I := \pi r^4/4$, E_s the Young's modulus of the lattice's constituent material and

$$
\begin{aligned}
&p_1 = 4d_1^2 + L_1^2 + L_2^2, \qquad p_2 = 4d_2^2 + L_1^2 + L_3^2, \qquad p_3 = 4d_3^2 + L_2^2 + L_3^2,\\
&p_4 = p_1^{5/2} p_2^{5/2} \left(L_2^2 + L_3^2\right), \qquad p_5 = p_2^{5/2} \left(4d_1^2 + L_2^2\right) + L_1^2 \left(p_1^{5/2} + p_2^{5/2}\right) + p_1^{5/2} \left(L_3^2 + 4d_2^2\right),\\
&p_6 = \left(p_2^{5/2} \left(4d_1^2 + L_2^2\right) + L_3^2 p_1^{5/2}\right),\\
&p_7 = \left(4d_2^2 L_1^2 p_1^{5/2} + \left(4d_1^2 + L_1^2\right) p_2^{5/2}\right) p_3^{5/2} + L_3^2 p_1^{5/2} \left(p_2^{5/2} + 4d_2^2 p_3^{5/2}\right),\\
&p_8 = 16d_2^4 \left(4d_2^2 + L_1^2 + L_3^2\right) p_1^{5/2} p_3^{5/2} + L_2^4 p_2^{5/2} \left(p_1^{5/2} + p_3^{5/2}\right),\\
&p_9 = L_2^2 p_2^{5/2} \left(L_3^2 p_1^{5/2} + \left(4d_1^2 + L_1^2\right) p_3^{5/2}\right), \qquad p_{10} = 16d_1^4 p_2^{3/2} p_3^{3/2} + L_3^2 p_1^{3/2} \left(p_2^{3/2} + p_3^{3/2}\right),\\
&p_{11} = \left(4d_2^2 p_1^{5/2} + L_1^2 \left(p_1^{5/2} + 4d_1^2 p_2^{5/2}\right)\right) p_3^{5/2} + L_2^2 p_2^{5/2} \left(p_1^{5/2} + 4d_1^2 p_3^{5/2}\right),\\
&p_{12} = \frac{16A\sqrt{p_1} + \sqrt{p_2} + \sqrt{p_3}}{\left(L_2 L_3\right)^2 \left(p_1 p_2 p_3\right)^{5/2}}.
\end{aligned}
\tag{27}
$$

Appendix C

References

F. Albertini, J. Dirrenberger, A. Molotnikov, and C. Sollogoub. Computational investigation of the effective mechanical behavior for 3D pre-buckled auxetic lattices. *Journal of Applied Mechanics*, 86:111003, 2019.

F. Albertini, J. Dirrenberger, C. Sollogoub, T. Maconachie, M. Leary, and A. Molotnikov. Experimental and computational analysis of the mechanical properties of composite auxetic lattice structures. *Additive Manufacturing*, 47:102351, 2021.

M. F. Ashby. Designing architectured materials. *Scripta Materialia*, 68(1):4–7, Jan. 2013.

ASTM. D638-14: Standard test method for tensile properties of plastics, 2014.

M. Born and K. Huang. *Dynamical Theory of Crystal Lattices*. Oxford University Press, 1954.

L. Brillouin. *Wave Propagation in Periodic Structures*. Dover, 1953.

A. Challapalli. Continuum model for effective properties of orthotropic octet-truss lattice through additive manufacturing. *International Journal for Computational Methods in Engineering Science and Mechanics*, 0:1–11, 2020. doi: 10.1080/15502287.2020.1711829.

J. Y. Chen, Y. Huang, and M. Ortiz. Fracture analysis of cellular materials: a strain gradient model. *Journal of the Mechanics and Physics of Solids*, 46(5):789–828,

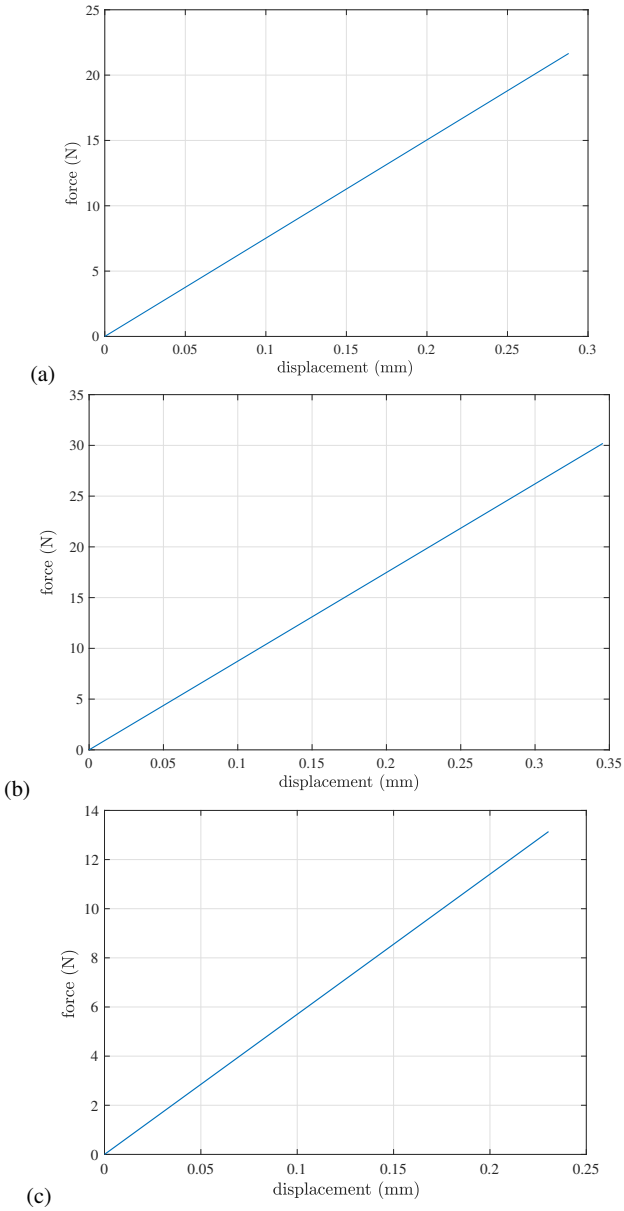

Fig. 4 PLA samples, compression tests: experimental force-displacement curves for (a) configuration C1, (b) configuration C2, (c) configuration C3

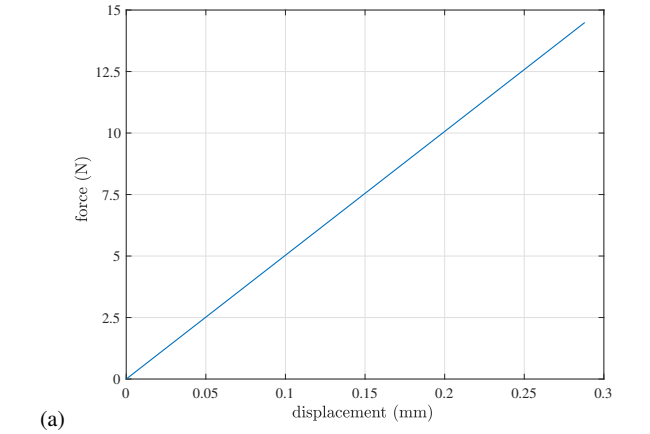

(a)

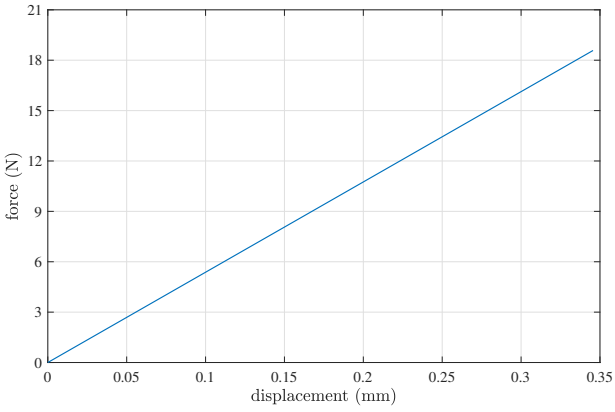

(b)

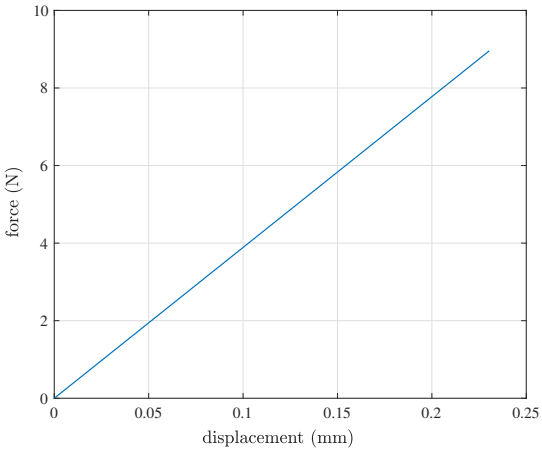

(c)

Fig. 5 PET samples, compression tests: experimental force-displacement curves for (a) configuration C1, (b) configuration C2, (c) configuration C3

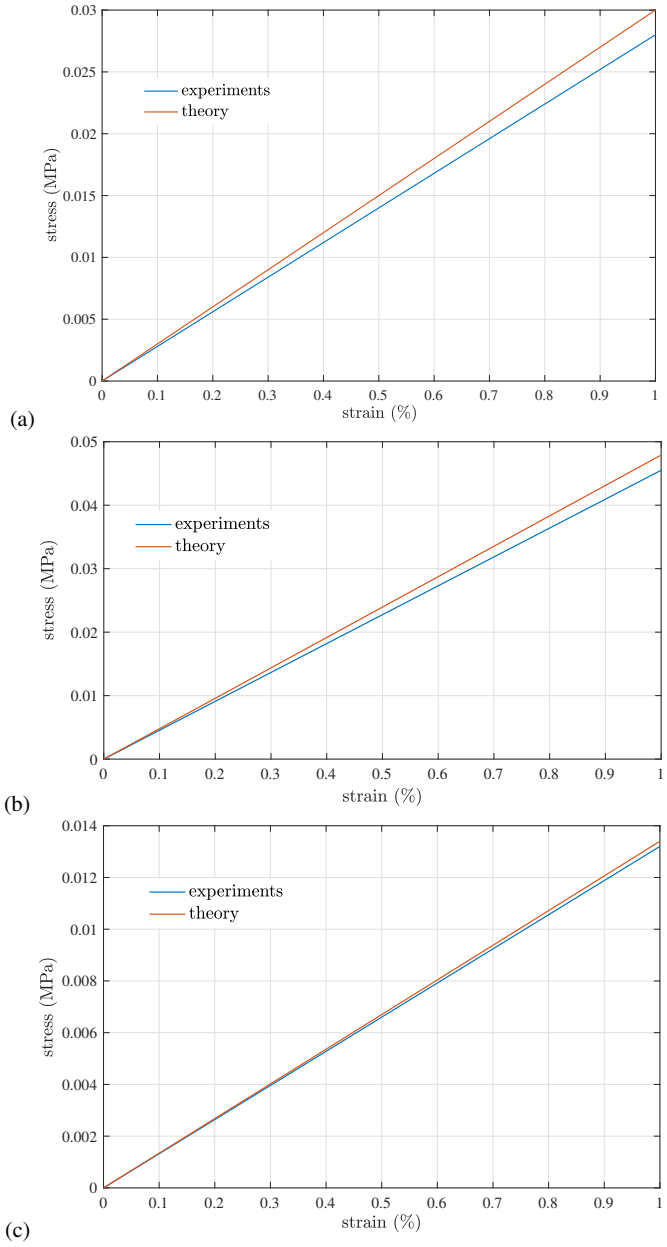

Fig. 6 PLA samples, compression tests: experimental stress-strain curves for (a) configuration C1, (b) configuration C2, (c) configuration C3

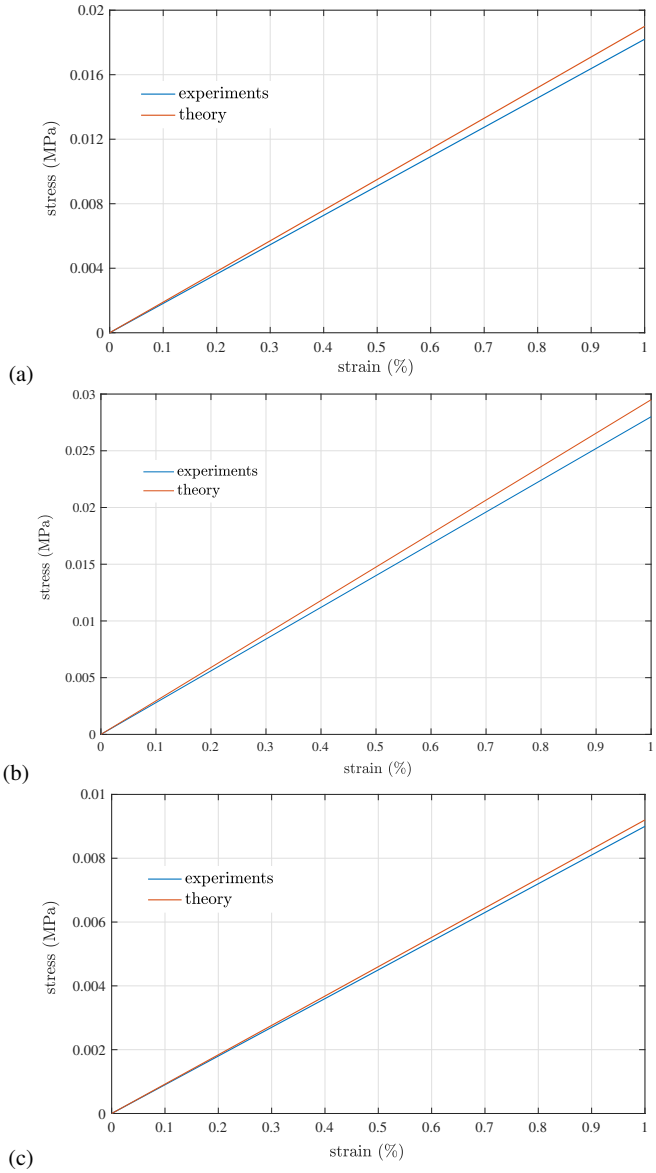

Fig. 7 PET samples, compression tests: experimental stress-strain curves for (a) configuration C1, (b) configuration C2, (c) configuration C3

1998.

R. M. Christensen. Mechanics of cellular and other low-density materials. *International Journal of Solids and Structures*, 37:93–104, 2000.

V. S. Deshpande, N. A. Fleck, and M. F. Ashby. Effective properties of the octet-truss lattice material. *Journal of the Mechanics and Physics of Solids*, 49(8): 1747–1769, 2001.

J. Dirrenberger, S. Forest, and D. Jeulin. Effective elastic properties of auxetic microstructures: anisotropy and structural applications. *International Journal of Mechanics and Materials in Design*, 9(1):21–33, Mar. 2013. doi: 10.1007/s10999-012-9192-8.

R. J. D'Mello and A. M. Waas. In-plane crush response and energy absorption of circular cell honeycomb filled with elastomer. *Composite Structures*, 106: 491–501, 2013.

M. S. Elsayed and D. Pasini. Analysis of the elastostatic specific stiffness of 2d stretching-dominated lattice materials. *Mechanics of Materials*, 42(7):709–725, 2010.

A. J. M. Ferreira. *MATLAB codes for finite element analysis*. Springer, 2009.

R. T. L. Ferreira, I. C. Amatte, T. A. Dutra, and D. Bürger. Experimental characterization and micrography of 3d printed pla and pla reinforced with short carbon fibers. *Composites Part B: Engineering*, 124:88–100, 2017.

L. J. Gibson. Modelling the mechanical behavior of cellular materials. *Materials Science and Engineering A*, 110:1–36, 1989.

L. J. Gibson and M. F. Ashby. *Cellular Solids*. Cambridge University Press, 2 edition, 1999.

S. Gonella and M. Ruzzene. Homogenization and equivalent in-plane properties of two-dimensional periodic lattices. *International Journal of Solids and Structures*, 45(10):2897–2915, 2008.

R. G. Hutchinson and N. A. Fleck. The structural performance of the periodic truss. *Journal of the Mechanics and Physics of Solids*, 54(4):756–782, 2006.

A. M. Kraynik, M. K. Neilsen, D. A. Reinelt, and W. E. Warren. Foam micromechanics. In *Foams and Emulsions: Proceedings of the NATO Advanced Study Institute on Foams, Emulsions and Cellular Materials*. Kluwer, 1998.

R. S. Kumar and D. L. McDowell. Generalized continuum modeling of 2-d periodic cellular solids. *International Journal of Solids and Structures*, 41:7399–7422, 2004.

S. Nemat-Nasser and M. Hori. *Micromechanics: Overall Properties of Heterogenous Materials*. North-Hollan d Publishing, 1993.

F. Ongaro, K. Mathis, F. Masson, and J. Dirrenberger. Architectured materials for space applications: a computational tool for the parametric optimization of a three-dimensional lattice subjected to stiffness constraints. In *8th European Conference for Aeronautics and Aerospace Sciences (EUCASS), 1-4 July 2019, Madrid, Spain*, 2019.

M. Ostoja-Starzewski. Lattice models in micromechanics. *Applied Mechanics Reviews*, 55(6):35–60, 2002.

K. Refai, M. Montemurro, C. Brugger, and N. Saintier. Determination of the effective elastic properties of titanium lattice structures. *Mechanics of Advanced Materials and Structures*, 27(23):1966–1982, 2020.

J. T. Seitz. The estimation of mechanical properties of polymers from molecular structure. *Journal of Applied Polymer Science*, 49:1331–1351, 1993.

A. Vigliotti and D. Pasini. Stiffness and strength of tridimensional periodic lattices. *Computer Methods in Applied Mechanics and Engineering*, 229:27–43, 2012a.

A. Vigliotti and D. Pasini. Linear multiscale analysis and finite element validation of stretching and bending dominated lattice materials. *Mechanics of Materials*, 46:57–68, 2012b.

A. Vigliotti and D. Pasini. Structural optimization of lattice materials. In *Proceedings of the ASME 2011*, 2012c.

W. E. Warren and A. M. Kraynik. Linear elastic behavior of a low-density kelvin foam with open cells. *Mechanics of Materials*, 64:787–794, 1997.

H. X. Zhu, J. F. Knott, and N. J. Mills. Analysis of the elastic properties of open-cell foams with tetrakaidecahedral cells. *Journal of the Mechanics and Physics of Solids*, 45:319–325, 1997.